



Truncated nonlocal kinetic energy density functionals for simple metals and siliconLiang Sun ¹, Yuanbo Li,¹ and Mohan Chen ^{1,2,*}¹*HEDPS, CAPT, School of Physics and College of Engineering, Peking University, Beijing 100871, People's Republic of China*²*AI for Science Institute, Beijing 100080, People's Republic of China*

(Received 3 April 2023; revised 31 July 2023; accepted 2 August 2023; published 24 August 2023)

The adoption of an accurate kinetic energy density functional (KEDF) to characterize the noninteracting kinetic energy within the framework of orbital-free density functional theory (OFDFT) is challenging. We propose a form of the nonlocal KEDF with a real-space truncation cutoff that satisfies the uniform electron gas limit and design KEDFs for simple metals and silicon. These KEDFs are obtained by minimizing a residual function, which contains the differences in the total energy and charge density of several representative systems with respect to the Kohn-Sham DFT results. By systematically testing different cutoffs of these KEDFs, we find that the cutoff plays a crucial role in determining the properties of metallic Al and semiconductor Si systems. We conclude that the KEDF with a sufficiently long cutoff performs even better than some representative non-local KEDFs in some aspects, which sheds light on optimizing the KEDFs in OFDFT to achieve better accuracy.

DOI: [10.1103/PhysRevB.108.075158](https://doi.org/10.1103/PhysRevB.108.075158)**I. INTRODUCTION**

Kohn-Sham density functional theory (KSDFT) is one of the most widely used *ab initio* methods [1,2]. However, since the traditional KSDFT method introduces orthogonal one-electron orbitals, solving the Kohn-Sham equation typically scales as $O(N^3)$, with N being the atom number, which is unfavorable for large-size calculations or long-time molecular dynamics simulations. Orbital-free DFT (OFDFT) [3,4] is an alternative choice to improve the efficiency of DFT by calculating the noninteracting electron kinetic energy T_s via the kinetic energy density functional (KEDF) instead of the one-electron Kohn-Sham orbitals. OFDFT has been successfully applied to a variety of scientific problems such as alloys, [4–9] liquid metals [10], quantum dots [11,12], and warm dense matter [13,14]. Recently, the time-dependent OFDFT has been proposed to study the stopping power of electrons in warm dense matter [15,16], the localized surface plasmon resonances in nanorods [17], and the optical spectra of metallic and semiconductor clusters [18]. Since the magnitude of electron kinetic energy (T_s) is comparable to the total energy in condensed matter and molecular systems, the accuracy of OFDFT is sensitive to the approximated forms of the KEDF. In this regard, proposing an accurate and efficient KEDF within the framework of OFDFT has been a challenging topic in this community for decades.

In the past few decades, continuous efforts have been devoted to the development of KEDFs. As a result, various forms of a KEDF have been proposed. A typical category of KEDFs includes the local and semilocal components, which can be efficiently evaluated. For instance, Constantin *et al.* demonstrated the importance of adopting the Laplacian of charge density in the construction of KEDFs and proposed

a series of new semilocal KEDFs [19,20]. Luo *et al.* generalized the Luo-Karasiev-Trickey (LKT) KEDF [21] to finite temperatures [22] and applied it to warm dense hydrogen [14]. The next category of KEDFs is the nonlocal form, which suggests that the kinetic density at each real-space point depends on the nonlocal charge density. For condensed matter systems, the nonlocal KEDFs are generally more accurate than the semilocal ones, such as the Wang-Teter (WT) [23], the Smargiassi-Madden (SM) [24], and the Wang-Govind-Carter (WGC) [25] KEDFs for metals and the Huang-Carter (HC) KEDF [26] for semiconductors. While most KEDFs were constructed based on the Lindhard response function, another category of KEDFs was introduced by imposing more restrictions or using more parameters; for example, the enhanced von Weizsäcker WGC KEDF [27], the KGAP KEDF based on the jellium-with-gap model [28], and the KEDFs in the form of functional integrals [29,30]. In particular, the revised HC KEDF [31] was proposed to achieve higher precision for the surface of semiconductors.

While most of the nonlocal KEDFs implement a nonlocal kinetic energy kernel, a fundamental yet important issue regarding how the long- and short-range parts of the kinetic energy kernel influence the accuracy of KEDFs is still unclear. In this regard, a truncated KEDF kernel (TKK) with a chosen real-space cutoff could provide further information for this issue. Recently, a truncated WT kernel was proposed [32] to enable efficient calculations of 1 024 000 lithium (Li) atoms with the OFDFT method. The truncated WT kernel is composed of eight spherical Bessel functions and yields reasonable results for Li systems. Note that the spherical Bessel functions have been used as localized basis sets in density functional theory calculations [33–36]. Similarly, Kumar *et al.* proposed a nonlocal KEDF whose kinetic energy kernel consists of six Gaussian functions and found improved performances for a series of one-dimensional systems [37]. In this regard, constructing a TKK that owns sufficient accuracy

*mohanchen@pku.edu.cn

within the framework of OFDFT has been demonstrated to be feasible; nevertheless, an important remaining issue is to reveal the influences of the long- and short-range parts of KEDF on a selection of target systems.

In this work, we construct two groups of TKK, i.e., one for metals (labeled $\text{TKK}_{\lambda_c}^m$, with λ_c being the real-space cutoff) and the other for semiconductors (labeled $\text{TKK}_{\lambda_c}^s$), because the asymptotic behaviors of KEDFs for metals and semiconductors are different [26]. In particular, as a first step to find an optimal KEDF for metals and another one for semiconductors, we respectively choose Al and Si to validate the two groups of TKKs. For each group, a few TKKs are represented by a set of spherical Bessel functions and generated [32] with different radius cutoffs. The coefficients of spherical Bessel functions are optimized with the simulated annealing method [38,39]. We systematically test these kernels for a variety of Al and Si systems. In general, the accuracy of TKKs increases with a larger cutoff. In particular, we find it crucial to consider the interactions between an atom and its nearest neighbors, as well as the next-nearest neighbors in a TKK; otherwise, the stacking fault energies and surface energies of Al, as well as the vacancy formation energies and surface energies of Si, are qualitatively incorrect. Additionally, the TKK_{16}^m kernel works well for Li and Mg bulk systems, demonstrating its transferability. The computational efficiency of TKKs is similar to the WT and WGC KEDFs, and higher than the HC KEDF.

The rest of this paper is organized as follows. In Sec. II, we introduce the method to optimize the truncated WT kernel. In Sec. III, we list the numerical details of the KSDFT and OFDFT calculations. In Sec. IV, we analyze the performances of the KEDF kernel presented here and discuss the results. Finally, the conclusions are drawn in Sec. V.

II. METHODS

A. Kinetic energy density functional kernel

The WT KEDF [23] is derived from the Lindhard response function and takes the form of

$$T_{\text{WT}}[\rho(\mathbf{r})] = C_{\text{TF}} \int \rho^{5/3}(\mathbf{r}) d\mathbf{r} + \frac{1}{8} \int \frac{|\nabla \rho(\mathbf{r})|^2}{\rho(\mathbf{r})} d\mathbf{r} + C_{\text{TF}} \iint \rho^\alpha(\mathbf{r}) W(\mathbf{r} - \mathbf{r}') \rho^\beta(\mathbf{r}') d\mathbf{r} d\mathbf{r}', \quad (1)$$

where $C_{\text{TF}} = \frac{3}{10}(3\pi^2)^{2/3}$. The parameters α and β are typically set to $5/6$. The first term is the Thomas-Fermi (TF) KEDF [40], which is a local functional exact for the uniform electron gas. The second term is the semilocal von Weizsäcker (vW) KEDF [41], which is a rigorous lower bound to the T_s . The last term is a nonlocal form of KEDF derived from the Lindhard response function, with $W(\mathbf{r} - \mathbf{r}')$ being the nonlocal KEDF kernel. Furthermore, the kernel can be analytically written in the reciprocal space as [23,25]

$$W(\eta) = \frac{5G(\eta)}{9\alpha\beta\rho_0^{\alpha+\beta-5/3}}, \quad (2)$$

where

$$G(\eta) = \left(\frac{1}{2} + \frac{1-\eta^2}{4\eta} \ln \left| \frac{1+\eta}{1-\eta} \right| \right)^{-1} - 3\eta^2 - 1. \quad (3)$$

Here, $\eta = \frac{k}{2k_{\text{F}}}$ is a dimensionless reciprocal space vector, while $k_{\text{F}} = (3\pi^2\rho_0)^{1/3}$ is the Fermi wave vector with ρ_0 being the average charge density. The truncated kinetic kernel is expressed as a linear combination of spherical Bessel functions and takes the form

$$W_{\text{T}}(\lambda) = \begin{cases} \sum_i c_i j_l(q_i \lambda), & \lambda < \lambda_c \\ 0, & \lambda \geq \lambda_c, \end{cases} \quad (4)$$

where $j_l(q_i \lambda)$ is a spherical Bessel function and c_i is the coefficient. The parameter q_i satisfies $j_l(q_i \lambda_c) = 0$. Here, the real-space cutoff is $\lambda_c = 2k_{\text{F}}|\mathbf{r} - \mathbf{r}'|$. The l parameter is set to 0, which is the same as in Ref. [32].

B. Residual function

With the aim of obtaining a more accurate KEDF kernel, we propose to optimize the coefficients of the spherical Bessel functions in Eq. (4) for a selected set of representative systems. In this regard, we define a residual function as

$$R = |\Delta E_{\text{tot}}| + \mu|\Delta E_{\text{H}}| + \nu|J| + \xi|G|, \quad (5)$$

where μ , ν , and ξ are the coefficients. Here the first term denotes the absolute total energy difference of a target system as calculated by the OFDFT and KSDFT methods, and the formula is as follows:

$$|\Delta E_{\text{tot}}| = \frac{1}{N} \sum_{j=1}^N |E_{\text{tot},j}^{\text{OF}} - E_{\text{tot},j}^{\text{KS}}|/n_j, \quad (6)$$

where $E_{\text{tot},j}^{\text{OF}}$ and $E_{\text{tot},j}^{\text{KS}}$ are the total energies of the j th system as computed by the OFDFT utilizing the truncated kinetic kernels and the KSDFT method, respectively. N is the number of selected reference systems and n_j is the number of atoms in the j th system.

In order to minimize the charge density difference, we add a second term to minimize the absolute energy difference of the Hartree energy term, which takes the form

$$|\Delta E_{\text{H}}| = \frac{1}{N} \sum_{j=1}^N |E_{\text{H},j}^{\text{OF}} - E_{\text{H},j}^{\text{KS}}|/n_j, \quad (7)$$

where $E_{\text{H},j}^{\text{OF}}$ and $E_{\text{H},j}^{\text{KS}}$ represent the Hartree energies from the OFDFT and KSDFT calculations, respectively; both Hartree energies can be computed from $\frac{1}{2} \iint \frac{\rho(\mathbf{r})\rho(\mathbf{r}')}{|\mathbf{r}-\mathbf{r}'|} d\mathbf{r} d\mathbf{r}'$, with $\rho(\mathbf{r})$ being the charge density.

In fact, in a uniform electron gas, the electron density remains a constant and the TF model is exact to describe the kinetic energy of electrons. In this case, the nonlocal term is expected to disappear and the TKK KEDF should be equivalent to the TF model. This implies that the integration of the nonlocal TKK should yield zero. In this regard, we impose a constraint in the third term J to satisfy the limit of uniform electron gas, which can be written as

$$J = \sum_{i=1}^{N_i} c_i \int_0^{\lambda_c} \lambda^2 j_0(q_i \lambda) d\lambda. \quad (8)$$

The term J is the integral of a TKK in real space, with N_i being the number of spherical Bessel functions. For a TKK

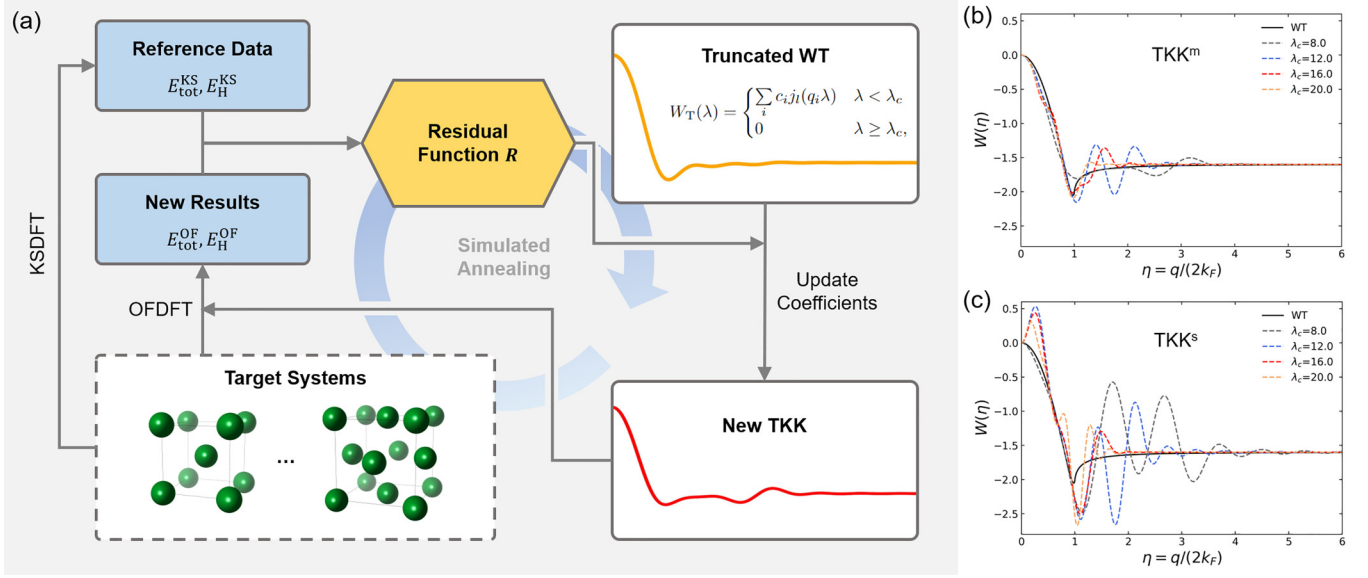


FIG. 1. (a) Workflow of the simulated annealing method to optimize the truncated KEDF kernel (TKK) in the framework of OFDFT. (b) The fitted TKKs in reciprocal space for metallic systems (labeled TKK^m) with the target systems being Al systems. The Wang-Teter (WT) KEDF kernel is plotted for comparison. The real-space cutoff λ_c is chosen with different values ranging from 8 to 20. (c) The fitted TKKs in reciprocal space for semiconductor systems (labeled TKK^s) with the target systems being Si systems.

that minimizes the residual function, the J term is supposed to be zero to satisfy the above-mentioned constraint.

Last, the fourth term, G , is included as a penalty term to reduce the oscillation behaviors of the truncated kinetic kernels and takes the form

$$G = \sum_{i=1}^{N_i} c_i \int_0^{\eta_c} \eta^4 \widehat{F}[j_0(q_i \lambda)] d\eta. \quad (9)$$

Here, \widehat{F} denotes the Fourier transform. The last term is added because we find that the resulting TKK kernel exhibits oscillating behavior in real space. Typically, the oscillating behavior can be effectively reduced in optimizing the shape of the function in reciprocal space. Therefore, we multiply the Fourier transform of the kernel function in reciprocal space by a η^4 term to reduce the oscillations, especially when the dimensionless reciprocal space vector η is large. In practice, we set the number of spherical Bessel functions to be $N_i = 8$ and the remaining parameters in Eq. (5), i.e., μ , ν , and ξ , are, respectively, set to 3, 1/10, and 1/20, so that the above four terms account for similar proportions of the residual.

C. Simulated annealing method

As illustrated in Fig. 1(a), we adopt the simulated annealing method to minimize the residual function R defined in Eq. (5). The workflow contains three steps. First, the KSDFT calculations are performed to yield the total energy $E_{\text{tot}}^{\text{KS}}$ and the Hartree energy E_{H}^{KS} of selected target systems as reference data. Second, starting from the truncated WT kernel, the coefficients $\{c_i\}$ of spherical Bessel functions are updated to obtain a different TKK $W_T(\lambda)$. We then use this TKK and perform OFDFT calculations for target systems to obtain the residual function R and the change of residual ΔR . Third, we use the *Metropolis* algorithm to update the coefficients $\{c_i\}$,

which means that the previously updated coefficient will be accepted if $\Delta R \leq 0$; or, if $\Delta R > 0$, the updated coefficients will be accepted with the probability $p = e^{-\Delta R/T}$, where T is the artificial temperature and gradually reduces during the optimization.

Note that we optimize two types of TKKs, including TKK^m [Fig. 1(b)] and TKK^s [Fig. 1(c)] for metals and semiconductors, respectively. The target systems are selected as follows. For the target metallic systems, we choose face-centered-cubic (fcc), body-centered-cubic (bcc), simple cubic (sc), and hexagonal close-packed (hcp) crystal structures of bulk Al. In addition, the fcc (111), (100), and (110) surfaces of Al are considered. We also adopt three different supercells ($1 \times 1 \times 1$, $2 \times 1 \times 1$, and $2 \times 2 \times 2$ supercells) of fcc Al, which contain one vacancy, to fit the vacancy formation energies. On the other hand, in the target systems for semiconductor systems, we select the cubic diamond (CD) and β -tin crystal structures of bulk Si. Moreover, we add the (100) surface of the CD Si and two different CD Si supercells containing one vacancy ($1 \times 1 \times 1$ and $2 \times 1 \times 1$ supercells) in the target systems.

During the optimization of TKKs, we impose a constraint during the optimization, which ensures the hydrodynamic limit ($\eta = 0$) of TKK to be fixed at zero, as in the conventional WT KEDF kernel $W(\eta)$ [32]. The optimization is performed for 10 temperatures by using the *Metropolis* algorithm, and 2100 and 1400 steps are carried out for each temperature for TKK^m and TKK^s KEDFs, respectively.

III. NUMERICAL DETAILS

We perform OFDFT and KSDFT calculations by using the PROFESS 3.0 [42] and ABACUS 2.1.0 [36] packages. The plane-wave energy cutoffs utilized in the OFDFT and KSDFT calculations for the above-mentioned systems, as well

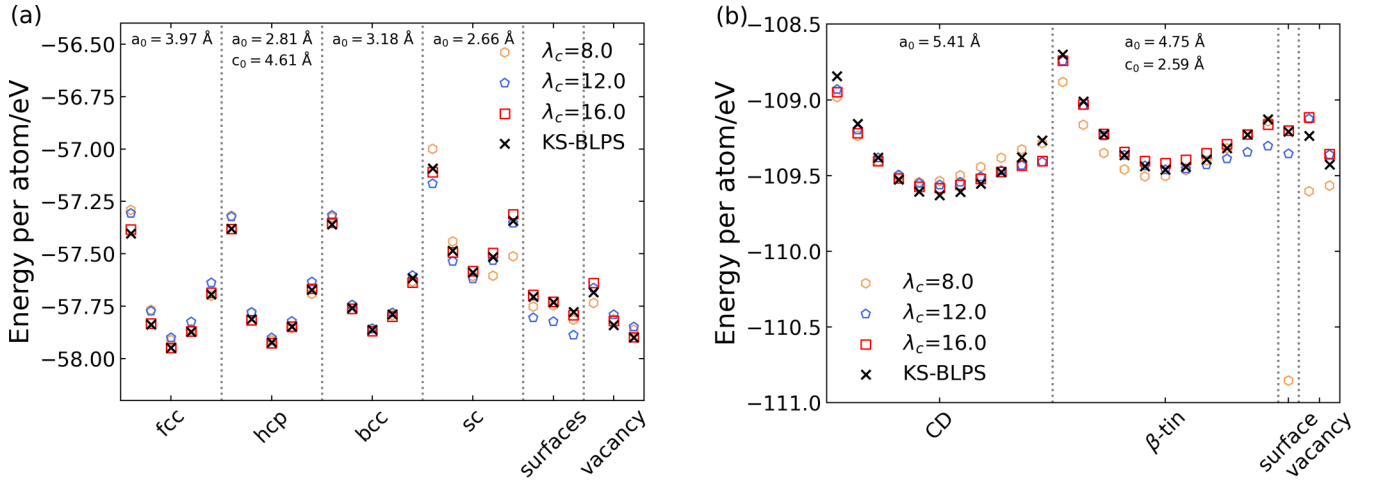


FIG. 2. Total energies (in eV/atom) of target systems as calculated by using the KS-BLPS and OFDFT methods. In OFDFT calculations, three different TKK kernels with the cutoff being $\lambda_c = 8, 12$, and 16 are chosen. The metallic systems are illustrated in (a), including the fcc, hcp, bcc, and sc crystal structures of Al, which are compressed and expanded with the equilibrium lattice constant a_0 ranging from $0.9a_0$ to $1.1a_0$, and five points are chosen for each structure. In addition, the Al fcc surfaces $[(110), (100), \text{ and } (111)]$ surfaces in turn, as well as the vacancy configurations ($1 \times 1 \times 1, 2 \times 1 \times 1$, and $2 \times 2 \times 2$ supercells in turn), are chosen. For the semiconductor systems shown in (b), we choose the cubic diamond (CD) and β -tin solid phases of Si (compress and expand the unit cell from $0.9a_0$ to $1.1a_0$ to obtain 11 points for each configuration), the CD (100) surface, and the CD vacancy configurations ($1 \times 1 \times 1$ and $2 \times 1 \times 1$ supercells in turn).

as the Monkhorst-Pack k -point samplings [43] in KSDFT, are listed in Table S1 in the Supplemental Material [50]. In both OFDFT and KSDFT calculations, the local density approximation (LDA) [44] and the bulk-derived local pseudopotentials (BLPS) [45] are used. In particular, the Gaussian smearing method is used in the KSDFT calculations for metallic systems, with a smearing width of 0.1 eV. In order to calculate the ground-state bulk properties, we first optimize the crystal structures until the stress tensor elements are below 5×10^{-7} Hartree/Bohr³, then compress and expand the unit cell from $0.99a_0$ to $1.01a_0$, where a_0 is the equilibrium lattice constant. Once the energy-volume curve is obtained, bulk modulus B is calculated by fitting Murnaghan's equation of state [46]. In order to assess the error of B , we choose two different sets of data for the fcc and hcp Al structures and adopt KSDFT with BLPS and the LDA functional. First, the lattice constant is chosen from $0.990a_0$ to $1.010a_0$. The calculated bulk moduli of fcc and hcp Al are 84 and 81 GPa, respectively. Second, we change the range of the lattice constant from $0.995a_0$ to $1.005a_0$, and the resulting bulk moduli are 83 and 81 GPa for the fcc Al and hcp Al, respectively. The two sets of data are close, suggesting that our method to estimate the bulk moduli is reasonably accurate.

We compare the TKK results to those obtained from OFDFT calculations with traditional KEDFs. In detail, the WT and WGC KEDFs are used for systems involving Al, Li, and Mg. The WT, WGC, and HC KEDFs are adopted for Si systems. We set $\alpha = \frac{5+\sqrt{5}}{6}$, $\beta = \frac{5-\sqrt{5}}{6}$, and $\gamma = 2.7$ in the WGC KEDF for Al, Li and Mg metals, which are the optimized parameters of the WGC KEDF as proposed in Ref. [25]. In addition, we choose $\alpha = \frac{5+\sqrt{5}}{6}$, $\beta = \frac{5-\sqrt{5}}{6}$, and $\gamma = 4.2$ for the Si systems, which are optimum for semiconductors, as suggested by Ref. [47]. The HC KEDF is chosen for Si with the parameters $\beta = 0.65$, $\lambda = 0.01$ for the CD structure and $\beta = 0.65$, $\lambda = 0.0055$ for the β -tin structure,

which is optimum for corresponding systems [26]. In all OFDFT calculations, we set the average charge density ρ_0 as the average charge density over the whole cell.

The Al fcc (111), (100), and (110) surfaces are, respectively, tested with five, five, and seven layers of atoms [25], while the Si CD(100) surface is modeled with nine layers of atoms [26]. In addition, each layer of the above slabs contains one atom, and the lattice vectors are fixed to the equilibrium bulk lattice vectors while the vacuum is set to be larger than 10 \AA . The surface energy σ is defined as

$$\sigma = \frac{E_{\text{slab}} - NE_0}{2A}, \quad (10)$$

where E_{slab} is the total energy of the slab, E_0 is the ground energy per atom of bulk fcc Al or CD Si, N is the number of atoms in the slab, and A is the lateral area of the slab.

The vacancy configurations of fcc Al (CD Si) are set up by removing one atom from a supercell, which is constructed by combining n Al fcc (Si CD) cubic unit cells together in a $n_1 \times n_2 \times n_3$ fashion with $n = n_1 n_2 n_3$. Next, the vacancy formation energy E_{vf} is calculated via [48]

$$E_{\text{vf}} = E\left(N-1, 1, \frac{N-1}{N}\Omega\right) - \frac{N-1}{N}E(N, 0, \Omega), \quad (11)$$

where $E(N, m, \Omega)$ is the total energy for a cell. The parameters Ω , N , and m depict the volume, the number of atoms, and the number of defects, respectively.

The mean absolute relative error (MARE) of property x is defined as

$$\text{MARE} = \frac{1}{N} \sum_i^N \left| \frac{x_i^{\text{OF}} - x_i^{\text{KS}}}{x_i^{\text{KS}}} \right|. \quad (12)$$

Here, N is the number of data points, and x_i^{OF} and x_i^{KS} are obtained from OFDFT and KSDFT, respectively.

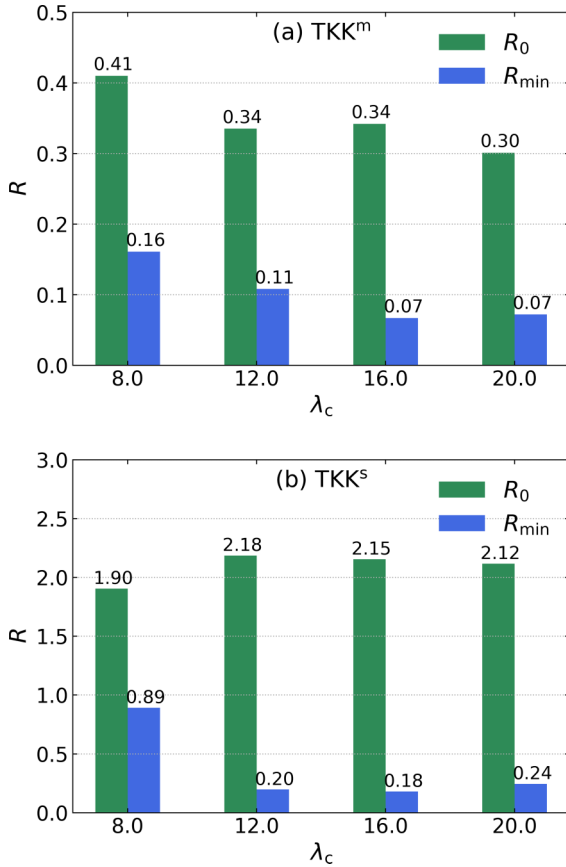


FIG. 3. Residual values [R_0 and R_{\min} in Eq. (5)] for the target systems before and after the optimization of the truncated KEDF kernel (TKK) with the simulated annealing method. The optimized TKKs are labeled TKK^m and TKK^s for the (a) metallic and (b) semiconductor systems, respectively. The dimensionless radial cutoff of the TKKs is λ_c . R_0 and R_{\min} are the original residuals before optimization and the minimum residual after optimization, respectively.

The stacking fault energies are calculated with the same setup as in Bernstein and Tadmor’s work [49]. More information, such as the computed stacking fault energies, is shown in Fig. S1 in the Supplemental Material [50].

IV. RESULTS AND DISCUSSION

We generate TKKs with different cutoffs, i.e., $\lambda_c = 8.0, 12.0, 16.0, 20.0$, for metallic and semiconductor systems, and the total energies of the target systems as obtained by KS-BLPS and OFDFT are shown in Fig. 2. We find that the total energies obtained by OFDFT get closer to those obtained by KS-BLPS as the cutoff of KEDF increases; the starting residual function R_0 (green bars) and the final residual function R_{\min} (blue bars) in terms of different cutoffs are shown in Fig. 3. We find that the final residual R_{\min} is substantially smaller than the original residual R_0 , implying that the optimization scheme is effective. Notably, as λ_c increases, the residual decreases first and then increases slightly. This may be caused by the introduction of the long-range part, which enhances the accuracy of TKK. However, as the λ_c increases, the fitting capability for the two TKKs reaches a saturation point.

TABLE I. Correspondence between the real-space distance (r_1 and r_2) and the real-space cutoff ($\lambda_1 = 2k_F r_1$ and $\lambda_2 = 2k_F r_2$) in the fcc Al, hcp Al, CD Si, and β -tin Si crystal systems. Here, r_1 (r_2) depicts the distance between an atom and its nearest neighbor (next-nearest neighbor), and $k_F = (3\pi^2\rho_0)^{1/3}$ (in \AA^{-1}) is the Fermi vector with ρ_0 the average charge density.

	ρ_0 (\AA^{-3})	k_F (\AA^{-1})	r_1 (\AA)	r_2 (\AA)	λ_1	λ_2
fcc Al	0.192	1.785	2.807	3.970	10.020	14.171
hcp Al	0.191	1.782	2.808	4.586	10.006	16.341
CD Si	0.202	1.815	2.342	3.824	8.502	13.883
β -tin Si	0.274	2.010	2.462	2.591	9.894	10.412

Furthermore, given that the parameter $\lambda = 2k_F|\mathbf{r} - \mathbf{r}'|$ is dimensionless, it should be noted that the same real-space cutoff λ_c may correspond to varying real-space distances when the Fermi vector k_F takes different values. To clarify this point, we list the correspondence between the real-space distance and the cutoff λ in Table I. Notably, when it comes to analyzing the behavior of Al and Si systems, it is crucial to take into account the interactions between atoms up to the second-nearest neighbor. This is because these interactions can have a significant impact on the overall properties of the systems. Specifically, TKKs only consider the nearest-neighbor atoms for hcp Al when λ_c is less than 16, but consider the atoms up to the second neighbors when λ_c is larger than 16. In summary, TKK^m₁₆ and TKK^s₁₆ take into account interactions up to the second-nearest neighbors, whereas other TKKs with $\lambda_c < 16$ exclude these interactions.

A. Simple metals

Table II lists the bulk properties of the fcc, hcp, bcc, and sc crystal structures of Al as obtained from KSDFT and various kinetic energy functionals adopted in OFDFT. The bulk properties include the bulk modulus, the equilibrium volume, and the total energy. When compared to the experimental data, we find that the KSDFT method with the usage of the BLPS yields a slightly larger bulk modulus and a smaller equilibrium volume for fcc Al, but the results are reasonable. In addition, both KSDFT and OFDFT (the WGC and WT KEDFs) calculations yield similar bulk properties for the four phases of Al, including the prediction of the fcc structure to be the most stable solid phase among the four solid structures.

It is worth mentioning that the energy difference between the hcp and fcc structures is as small as 0.020, 0.018, and 0.027 eV/atom, which is obtained from the WT, WGC, and KS-BLPS calculations, respectively. Notably, the TKK^m _{λ_c} in OFDFT exhibits different levels of accuracy for the bulk properties of solid Al phases in terms of the dimensionless radial cutoff λ_c . In general, a higher accuracy of TKK^m _{λ_c} is obtained while λ_c increases from 8 to 16, approaching the accuracy of the WT/WGC KEDF. Interestingly, we notice that the energy difference between the hcp and fcc structures as obtained from TKK^m₈, TKK^m₁₂, and TKK^m₁₆ is 0.000, 0.000, and 0.021 eV/atom, respectively. The results indicate that the TKK^m _{λ_c} with $\lambda_c = 8$ or 12 predicts the same energy for fcc and hcp structures. In addition, we note that the small energy difference between the fcc and hcp Al structures predicted by KSDFT-BLPS with the LDA functional and KSDFT-BLPS

TABLE II. Bulk properties of the fcc, hcp, bcc, and sc crystal structures of Al, i.e., the bulk modulus (B in GPa), the equilibrium volume (V_0 in $\text{\AA}^3/\text{atom}$), and the energy of a given system (E_0 in eV/atom). The energy (E_0) of fcc Al is chosen to be the total energy, while the other energy terms are set as the energy difference between the fcc Al and other structures. The MARE as defined in Eq. (12) is obtained by comparing the OFDFT to KS-BLPS results. Both KSDFT and OFDFT calculations are performed with the use of bulk-derived pseudopotentials (BLPS). For OFDFT calculations, we use the WT KEDF and the TKKs for metals with different cutoffs λ_c (labeled $\text{TKK}_{\lambda_c}^m$). Some of the KS-BLPS and WGC KEDF data are taken from Ref. [45]. The experimental data of bulk moduli and equilibrium volumes for fcc Al are shown for comparison.

		fcc	hcp	bcc	sc	MARE
B (GPa)	KS-BLPS (this work)	84	81	77	66	
	KS-BLPS [45]	84	81	76	64	
	WGC [45]	81	80	75	62	3.11%
	WT	85	83	77	65	1.72%
	TKK_{16}^m	87	85	76	69	3.99%
	TKK_{12}^m	89	88	81	68	5.88%
	TKK_8^m	80	80	75	47	9.01%
	Expt. [51]	76.2				
V_0 (\AA^3)	KS-BLPS (this work)	15.644	15.741	16.084	18.797	
	KS-BLPS [45]	15.623	15.767	16.063	18.825	
	WGC [45]	15.632	15.764	15.887	19.223	0.93%
	WT	15.821	15.928	16.223	18.774	0.83%
	TKK_{16}^m	15.646	15.712	16.117	18.568	0.41%
	TKK_{12}^m	15.729	15.777	16.107	18.507	0.61%
	TKK_8^m	16.005	15.997	16.192	20.130	2.92%
	Expt. [52]	16.363				
E_0 (eV)	KS-BLPS (this work)	-57.949	0.027	0.087	0.361	
	KS-BLPS [45]	-57.955	0.038	0.087	0.362	
	WGC [45]	-57.941	0.018	0.079	0.354	0.00%
	WT	-57.934	0.020	0.078	0.335	0.02%
	TKK_{16}^m	-57.949	0.021	0.080	0.366	0.01%
	TKK_{12}^m	-57.900	0.000	0.043	0.280	0.05%
	TKK_8^m	-57.914	0.000	0.057	0.293	0.04%

with the Perdew-Burke-Ernzerhof (PBE) functional is quite close, which is 0.027 and 0.025 eV/atom, respectively.

As explained in Table I, the results suggest that the relatively short-range TKKs of $\lambda_c = 8$ or 12, which involve only the nearest neighbors, are not able to distinguish the subtle energy difference between the fcc and hcp structures of Al. The reason is because the two structures have similar local structures, which are closely packed planes of atoms, and they own the same atomic packing factor of 0.74 and the same coordination number of 12. Notably, we emphasize that the TKK_{16}^m KEDF with $\lambda_c = 16$, which involves the second-nearest neighbors, yields a satisfactory value of 0.021 eV/atom for the energy difference between the hcp and fcc structures. In addition, the bulk moduli and equilibrium volumes of the four structures of Al, as obtained from the TKK_{16}^m KEDF, match better with the KS-BLPS data as compared to those obtained from TKK_8^m and TKK_{12}^m . This can be seen by comparing the MARE.

To validate the transferability of TKKs, we perform OFDFT calculations of the stacking fault energies of fcc Al, which are crucial mechanical properties of metals, and the results are shown in Fig. 4. Notably, most OFDFT calculations yield smaller stacking fault energies than KSDFT. In particular, the TKK KEDFs with a small λ_c (8 and 12) yield incorrect intrinsic stacking fault energy γ_{isf} and extrinsic stacking fault energy γ_{esf} close to zero. This can be explained

by their inability to distinguish between the hcp and fcc crystal structures since the atoms near the stacking fault plane of fcc Al are arranged in the hcp configuration. Interestingly, when the cutoff of TKK increases to the second-nearest neighbor,

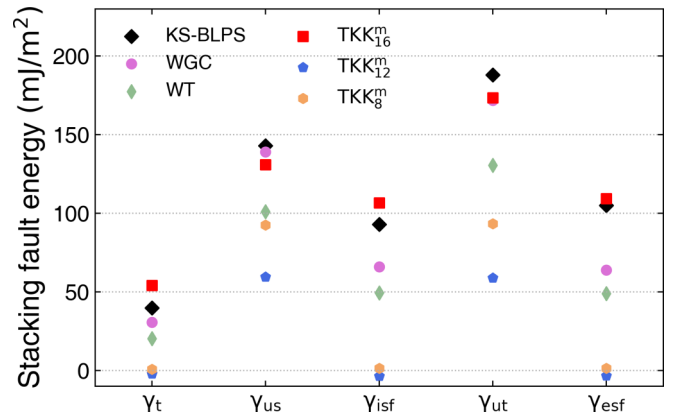


FIG. 4. Stacking fault energies (in mJ/m^2) of Al as obtained from KS-BLPS [45] and OFDFT calculations. The stacking fault energies include the twinning energy γ_t , the unstable stacking fault energy γ_{us} , the intrinsic stacking fault energy γ_{isf} , the unstable twinning energy γ_{ut} , and the extrinsic stacking fault energy γ_{esf} of fcc Al. The definition and explanation of the above five stacking fault energies can be found in Ref. [49].

TABLE III. OFDFT and KSDFT results for bulk modulus (B in GPa), equilibrium volume (V_0 in \AA^3 per atom), and total energy (E_0 in eV per atom) of various solid phases of Li and Mg. The last column is MARE (%). The equilibrium total energies of bcc Li and hcp Mg are given, while the energy differences are shown for other structures. All results of KSDFT and WGC KEDF for Mg are taken from Ref. [45].

Li		bcc	fcc	sc	CD	MARE
B (GPa)	KS-BLPS	17	17	17	12	
	WGC	17	17	17	12	0.15
	WT	17	17	17	12	0.15
	TKK_{16}^m	17	18	17	12	0.70
V_0 (\AA^3)	KS-BLPS	18.767	18.693	19.441	21.929	
	WGC	18.810	18.728	19.528	21.956	0.25
	WT	18.796	18.714	19.495	21.980	0.19
	TKK_{16}^m	18.699	18.628	19.474	21.989	0.29
E_0 (eV)	KS-BLPS	-7.599	-0.0004	0.139	0.538	
	WGC	-7.595	-0.002	0.140	0.535	0.04
	WT	-7.595	-0.002	0.140	0.536	0.04
	TKK_{16}^m	-7.599	-0.003	0.145	0.543	0.05
Mg		hcp	fcc	bcc	sc	MARE
B (GPa)	KS-BLPS [45]	38	38	37	29	
	WGC [45]	36	36	36	28	4.15
	WT	37	36	36	29	2.54
	TKK_{16}^m	37	37	36	29	2.02
V_0 (\AA^3)	KS-BLPS [45]	21.176	21.363	21.393	24.929	
	WGC [45]	21.616	21.465	21.534	25.036	0.91
	WT	21.358	21.533	21.590	25.006	0.72
	TKK_{16}^m	21.246	21.312	21.384	24.933	0.16
E_0 (eV)	KS-BLPS [45]	-24.678	0.011	0.033	0.370	
	WGC [45]	-24.651	0.006	0.024	0.351	0.08
	WT	-24.654	0.010	0.032	0.352	0.08
	TKK_{16}^m	-24.652	0.007	0.027	0.337	0.08

we observe that the TKK_{16}^m KEDF yields reasonable stacking fault energies, which are even better than those obtained from the WT and WGC KEDFs. Since the TKK_{16}^m function has a larger real-space cutoff than the TKK_8^m and TKK_{12}^m functions, we conclude that the long-range part in the real-space form of the TKK function is important to distinguish the energy difference between the fcc and hcp structures of Al, which is crucial to obtain reasonable stacking fault energies. The transferability of the proposed KEDF is verified in Table III, which will be discussed later.

As listed in Table IV, the surface energies of the Al fcc (100), (110), and (111) surfaces are computed by both OFDFT and KSDFT with the usage of BLPS. We find that the WT KEDF significantly overestimates the surface energies as compared to the KSDFT data. In detail, the KSDFT predicts the surface energies of Al to be 1010, 1104, and 1212 mJ/m^2 for the fcc (111), (100), and (110) surfaces, respectively; the WT KEDF yields surface energy of 1808, 1971, and 1996 mJ/m^2 for the fcc (111), (100), and (110) surfaces, respectively. Furthermore, the WGC KEDF largely improves the data, giving rise to a surface energy of 1176, 1373, and 1378 mJ/m^2 for the fcc (111), (100), and (110) surfaces, respectively. In terms of the TKKs with different cutoffs, the TKK_8^m and TKK_{12}^m KEDFs predict significantly smaller values for the surface energies of fcc Al as compared to the KSDFT data, which may be due to the short-range features of the two kinetic energy kernels in describing the kinetic energies of

electrons. Notably, the TKK_{16}^m KEDF not only predicts the surface energies of fcc Al close to the KSDFT results, but also yields the correct energy orderings for the three surfaces of fcc Al.

Table IV lists the vacancy formation energies of Al. First of all, the results obtained by the WT KEDF are substantially larger than the KSDFT data. For example, the vacancy formation energy of a $2 \times 2 \times 2$ cell is 1.447 and 0.794 eV from the WT and KS-BLPS calculations, respectively. The WGC KEDF is able to improve the value to 0.874 eV, which is closer to KSDFT. Second, we observe that all three TKK^m KEDFs yield a higher level of accuracy for the vacancy formation energies than the WT KEDF. Among them, the TKK_{12}^m KEDF performs best for all of the studied system sizes. Figure S2(a) in the Supplemental Material [50] shows the convergence behaviors of the vacancy formation energy with respect to the system size. We find that the TKK_{12}^m and TKK_8^m KEDFs exhibit a higher accuracy in predicting the vacancy formation energy in large systems compared to TKK_{16}^m KEDF, which may be attributed to the lack of sufficiently large supercells with vacancies in the target systems.

Figures 5(a) and 5(c), respectively, illustrate the electron densities of bulk fcc Al and its (100) surface as obtained from KSDFT and OFDFT calculations, and we choose the (010) surface of bulk Al to plot the electron density profile. For the bulk Al, the electron density differences between the OFDFT and KSDFT calculations and the associated MAREs

TABLE IV. Surface energies (σ , in mJ/m^2) and vacancy formation energies (E_{vf} , in eV) of fcc Al and CD Si. The BLPS of Al and Si are used in both the KSDFT and OFDFT calculations.

Al	Systems	KS-BLPS	WGC	WT	TKK_{16}^m	TKK_{12}^m	TKK_8^m
σ	Al fcc (111)	1010 ^a	1176	1808	919	81	584
	Al fcc (100)	1104 ^a	1373	1971	1117	394	848
	Al fcc (110)	1212 ^a	1378	1996	1276	485	813
E_{vf}^b	Al $1 \times 1 \times 1$	0.796	0.706	1.237	0.931	0.725	0.574
	Al $2 \times 1 \times 1$	0.757	0.740	1.347	0.905	0.786	0.751
	Al $2 \times 2 \times 1$	0.747	0.809	1.407	0.769	0.794	0.799
	Al $2 \times 2 \times 2$	0.794	0.874	1.447	0.592	0.763	0.791
Si	Systems	KS-BLPS	HC	WT	TKK_{16}^s	TKK_{12}^s	TKK_8^s
σ	Si CD (100)	2062	2548	-7824	2228	1307	-6172
E_{vf}^c	Si $1 \times 1 \times 1$	2.735	2.651	-0.572	3.277	3.081	-0.552
	Si $2 \times 1 \times 1$	3.026	2.313	-0.453	3.367	3.024	-0.551
	Si $2 \times 2 \times 2$	3.240	1.445	-0.346	3.583	3.143	-0.575

^aReference [45].

^bThe experimental value is 0.66 eV [53].

^cThe experimental value is 3.6 eV [54,55].

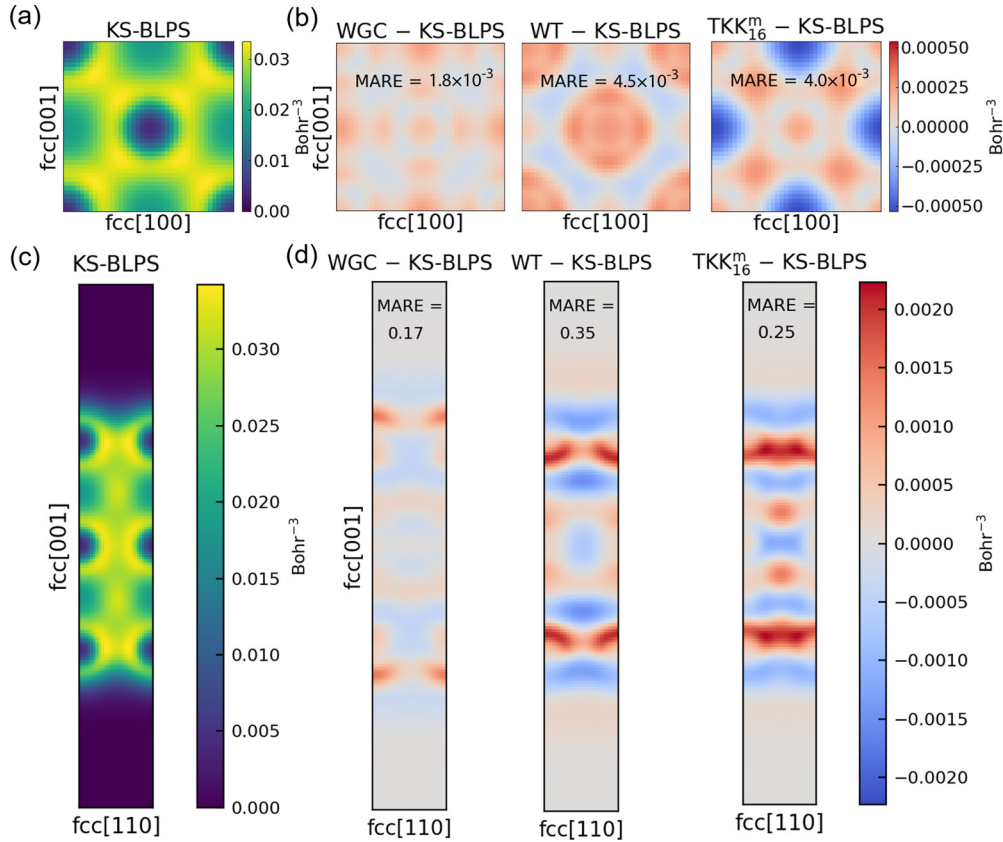


FIG. 5. (a) Electron density profile of the (010) crystal surface inside bulk fcc Al, which is obtained from KS-BLPS calculations. (b) Electron density differences of the fcc Al (010) crystal surface between OFDFT and KSDFT calculations. (c) Electron density profile on the longitudinal section of the Al fcc (100) surface, i.e., the fcc ($1\bar{1}0$) surface. Results are obtained from KSDFT calculations. Figure S3(a) of the Supplemental Material [50] shows the slab configuration. (d) Electron density differences of the Al fcc (100) surface between OFDFT and KSDFT calculations. We perform KSDFT calculations to obtain the equilibrium configuration used in the above calculations. The HC, WT, and TKK_{16}^s KEDFs are adopted in OFDFT. The MAREs, as defined in Eq. (12), of density differences shown in the figures are calculated from the whole electron density in the cell for bulk fcc Al and Al fcc (100) surface.

are displayed in Fig. 5(b). We observe that the WGC, WT, and TKK_{16}^m KEDFs are capable of reproducing the ground-state charge density obtained by KSDFT, with MAREs on the same order of 0.001 (0.0018, 0.0045, 0.0040 in turn). On the other hand, when dealing with the Al fcc (100) surface, we found the small electron density in vacuum may result in a large contribution to the MARE as defined in Eq. (12). Therefore, we did not calculate the contributions to MARE for a selected length of vacuum (5.2 Å) in the Al slab. The resulting MAREs of the Al fcc (100) surface are 0.17, 0.35, and 0.25 for the WGC, WT, and TKK_{16}^m KEDFs, respectively. We observe that the MAREs of the fcc (100) surface are still two orders of magnitude larger than those of the Al fcc bulk system. This phenomenon can be rationalized by the fact that the KEDFs are based on the Lindhard response function, which is suitable for describing Al bulk systems with electron density distribution similar to the uniform electron gas. However, when applied to Al surfaces, the electron density changes rapidly around the surfaces and substantially deviates from the uniform electron gas, resulting in a large MARE. Still, we find that the TKK_{16}^m KEDF achieves a similar accuracy when compared to the WGC and WT KEDFs, demonstrating that the TKK_{16}^m KEDF is able to accurately describe the electronic structure of metallic systems.

In order to assess the transferability of TKK_{16}^m KEDF, we conduct bulk property calculations for various solid phases of Li and Mg. The results are compared with those obtained from WGC, WT KEDFs, and KSDFT, which are presented in Table III. Since Li and Mg are simple metals, in which the electrons are nearly free electron gas, Lindhard-based KEDFs, such as WGC and WT KEDFs, are suitable to deal with them. As expected, the MAREs of energies obtained by WGC and WT KEDFs are of the order of 0.01 for both Li and Mg systems. In particular, the results obtained by the TKK_{16}^m KEDF are close to those obtained by KSDFT, and the MAREs are also comparable to those obtained by WGC and WT KEDFs. Notably, the TKK_{16}^m KEDF is able to reproduce the slight energy difference between different configurations, such as the energy difference of 0.007 eV/atom between the fcc and hcp Mg structures, which is close to the value of 0.011 eV/atom obtained by KSDFT. Overall, these findings highlight the excellent transferability of TKK_{16}^m KEDF for simple metals. Additionally, TKK_{16}^m KEDF also shows good transferability for Mg-Al alloys, and one can refer to the Supplemental Material [50].

It would be very interesting to study transition metals using orbital-free DFT. However, only a few works have tried to tackle transition metals and two challenges still remain. First, the framework of OFDFT can hardly handle the localized d electrons and new methods are needed. For example, the electron density decomposition method was proposed to examine Cu and Ag [56]. In addition, angular-momentum-dependent OFDFT was proposed to investigate Ti [57,58]. Second, well-tested local pseudopotentials for transition metals are still needed.

B. Silicon

Table V lists the bulk properties of CD and β -tin crystal structures of Si as obtained by KSDFT and OFDFT with

various KEDFs, where the CD Si is a typical semiconductor. For the bulk modulus of CD Si, the KS-BLPS calculations yield a value of around 99 GPa, which is in excellent agreement with the experimental data of 98.0 GPa. Meanwhile, the KS-BLPS predicts the equilibrium volume to be $19.774 \text{ \AA}^3/\text{atom}$, which is 1.19% smaller than the experimental value of $20.013 \text{ \AA}^3/\text{atom}$. Based on the data, we conclude that the KS-BLPS results are reasonable.

For the OFDFT calculations, since the WT KEDF is designed for free-electron-like systems, it is not surprising that the WT KEDF fails to calculate the bulk properties of the CD Si structure. Therefore, no WT results are included in Table V. In this regard, we utilize the more sophisticated WGC KEDF, which yields a substantially smaller bulk modulus of 54 GPa as compared to the experimental value of 98.0 GPa. Worse still, the equilibrium volume from WGC is $21.504 \text{ \AA}^3/\text{atom}$, which is 7.45% larger than the experimental value. In addition, we list the results of the HC KEDF taken from Ref. [26]. The HC is designed for semiconductors and performs significantly better than the WGC KEDF for the tested properties of CD Si. Unfortunately, the HC KEDF yields a worse bulk modulus and equilibrium volume for the β -tin structure when compared to WGC.

Notably, the energy difference between the CD and β -tin Si obtained from the HC KEDF (0.170 eV/atom) is close to the one from KS-BLPS (0.168 eV/atom), while the WGC KEDF yields a much smaller one of 0.016 eV/atom. By utilizing the $\text{TKK}_{\lambda_c}^s$'s with the increase of the cutoff from 8 to 16, we observe that the energy difference between CD and β -tin Si changes from 0.035 to 0.165 eV/atom, approaching the results of KSDFT (0.168 eV/atom). Although the TKK_{16}^s KEDF yields a worse bulk modulus of CD Si (78 GPa) than the HC KEDF (97 GPa), it performs better (110 GPa) than the HC (83 GPa) for the β -tin Si. In addition, the equilibrium volume of the β -tin Si structure is 14.482 and $15.662 \text{ \AA}^3/\text{atom}$ from the TKK_{16}^s KEDF and the HC KEDF, respectively; the former one is substantially closer to the $14.621 \text{ \AA}^3/\text{atom}$ as obtained from KS-BLPS calculations in this work. Regarding the KEDFs proposed in this work, we observe that all three $\text{TKK}_{\lambda_c}^s$'s perform better than the WGC KEDF, which is evidenced by the substantially smaller MARE in all three properties, including the bulk modulus, the equilibrium volume, and the total energy. This demonstrates that the TKK_{16}^s KEDF exhibits a better balance to describe the two phases of Si than the HC KEDF, and the long-range part of TKK plays a crucial role in determining the accuracy of nonlocal KEDF.

The surface energies and vacancy formation energies of Si are shown in Table IV. Since the Si systems own more localized electrons than the Al systems, and the corresponding surfaces involve the presence of a vacuum, it is not surprising that the Lindhard-based KEDFs cannot yield reasonable results for surfaces or vacancies of Si, as previous works have demonstrated this. For example, we encounter convergence issues with the WGC KEDF when dealing with the surface and vacancy of CD Si. Worse still, we find that the WT and the TKK_8^s KEDFs predict negative surface energies and vacancy formation energies, which are qualitatively incorrect values as compared to the KSDFT data. Interestingly, the TKK_{16}^s KEDF yields close values as compared to the KS-BLPS method. In detail, the TKK_{16}^s

TABLE V. Bulk properties of the cubic diamond (CD) and β -tin crystal structures of Si, i.e., the bulk modulus (B in GPa), the equilibrium volume (V_0 in $\text{\AA}^3/\text{atom}$), and the energy of a given system (E_0 in eV/atom), as well as available experimental data. The MARE, as defined in Eq. (12), is given by comparing OFDFT to KS-BLPS results. We set the E_0 to be the total energy for the CD structure, while the value for the β -tin is set to the energy difference with respect to the total energy of CD Si. Both the KSDFT and OFDFT calculations are performed with the use of bulk-derived pseudopotentials (BLPS). For OFDFT calculations, we use the WGC and HC KEDFs, as well as the TKKs for semiconductors with different cutoffs λ_c (labeled as $\text{TKK}_{\lambda_c}^s$).

		CD	β -tin	MARE
B (GPa)	KS-BLPS (this work)	99	123	
	KS-BLPS (Ref. [45])	98	122	
	HC (Ref. [26])	97	83	17.18%
	WGC	54	140	29.40%
	TKK_{16}^s	78	110	15.86%
	TKK_{12}^s	74	87	27.25%
	TKK_8^s	93	132	6.45%
	V_0 (\AA^3)	Expt. (Ref. [59])	98.0	
KS-BLPS (this work)		19.774	14.621	
KS-BLPS (Ref. [45])		19.777	14.663	
HC (Ref. [26])		19.962	15.662	4.04%
WGC		21.504	14.406	5.11%
TKK_{16}^s		19.470	14.482	1.24%
TKK_{12}^s		19.540	14.860	1.41%
TKK_8^s		18.974	14.133	3.69%
Expt. (Ref. [59])		20.013		
E_0 (eV)	KS-BLPS (this work)	-109.629	0.168	
	KS-BLPS (Ref. [45])	-109.629	0.166	
	HC (Ref. [26])	-109.624	0.170	0.01%
	WGC	-109.332	0.016	0.2%
	TKK_{16}^s	-109.583	0.165	0.04%
	TKK_{12}^s	-109.562	0.100	0.03%
	TKK_8^s	-109.545	0.035	0.06%

(KS-BLPS) predicts the CD Si (100) surface energy and the vacancy formation energy (in a $2 \times 2 \times 2$ cell) in the CD Si phase as 2228 (2062) mJ/m² and 3.583 (3.240) eV, respectively. The TKK_{16}^s KEDF performs substantially better than the HC KEDF, the latter of which predicts the vacancy formation energy as 1.445 eV. In addition, TKK_{12}^s also yields a reasonable vacancy formation energy of 3.143 eV, but a lower surface energy of 1307 mJ/m². Therefore, we conclude that the TKK_{16}^s performs better than the WT, WGC, and HC KEDFs for the surface energy and vacancy formation energy of Si. We plot the convergence trend of vacancy energies with respect to system size in Fig. S2 of the Supplemental Material [50]. We notice that in systems containing over 100 atoms, the results obtained through the TKK_{16}^s KEDF are almost indistinguishable from those obtained through KSDFT. The results again demonstrate the excellent performance of the TKK_{16}^s KEDF.

We further compare the electron density differences of bulk CD Si and its (100) surface as obtained from OFDFT and KSDFT calculations, which are displayed in Fig. 6. Note that we choose the (010) crystal surface of a bulk Si configuration to represent the electron density differences of bulk Si. The representative electron density profiles of the bulk Si and the (1 $\bar{1}$ 0) surface of Si are shown in Figs. 6(a) and 6(c), respectively. As shown in Fig. 6(b), the MAREs of electron density in bulk CD Si as obtained from the HC, WT, and TKK_{16}^s

KEDFs are 0.07, 0.12, and 0.10, respectively. The results are two orders of magnitude larger than those in bulk fcc Al, indicating that the electronic structure of semiconductors is more challenging to describe by KEDFs than the metallic ones. Figure 6(d) illustrates the electron density differences on the longitudinal section of the Si CD (100) surface, as well as the MAREs. As explained before, small electron density in vacuum may result in a large contribution to the MARE defined in Eq. (12), so we did not calculate the contributions to MARE for a selected length of vacuum (6.0 \AA) in the Si slab. As a result, we find the MAREs obtained by the HC, WT, and TKK_{16}^s KEDFs are 0.18, 0.14, and 0.16, respectively. We notice that the MAREs of a surface system and bulk system are of the same order of magnitude. The MAREs of the Si CD (100) surface are slightly larger than those of bulk CD Si. This can be explained by the fact that most KEDFs are not suitable for describing the covalent bonds of Si formed by electrons. From Fig. 6(d), we also observe that the WT and TKK_{16}^s KEDFs share a similar pattern of electron density differences. In the future, one can test the revHC KEDF [31] and see its performance for the above tests. Although the WT KEDF gives a better electron density, it predicts qualitatively wrong surface energy and vacancy formation energies, as listed in Table IV. Among the three KEDFs, both HC and TKK_{16}^s KEDFs are capable of capturing both the energies and the electron density with similar accuracy to KSDFT.

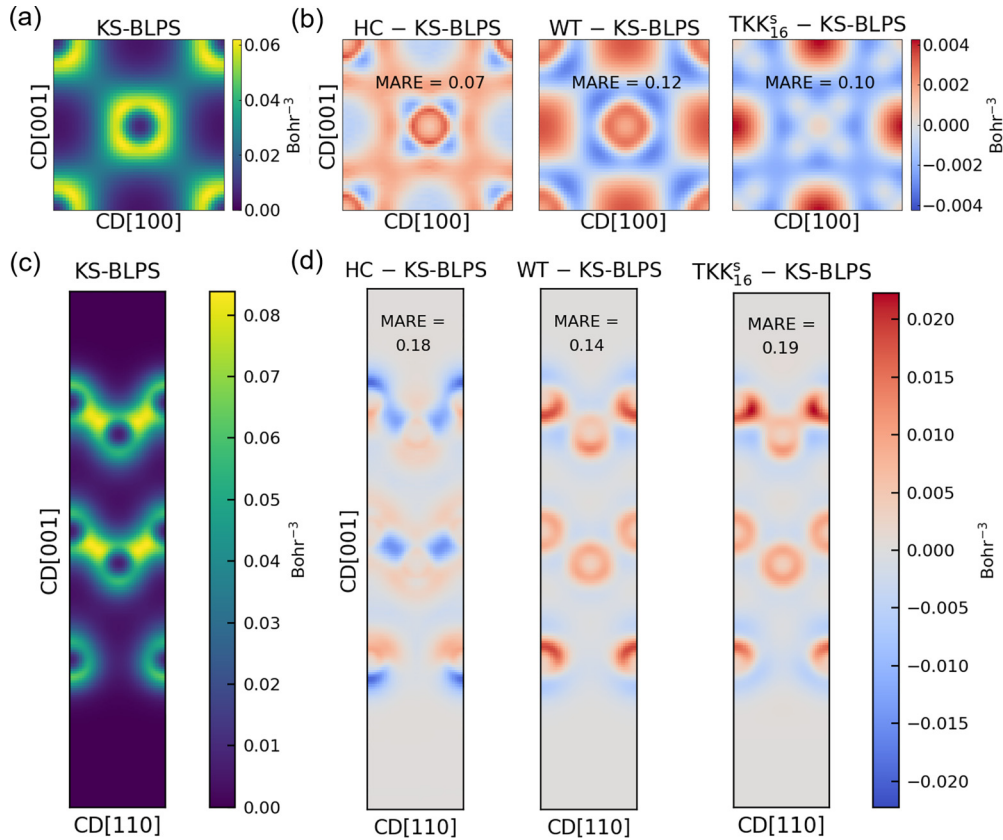


FIG. 6. (a) Electron density profile of the (010) crystal surface inside bulk CD Si as obtained from KSDFT. (b) Electron density differences of the CD Si (010) crystal surface between OFDFT and KSDFT calculations. (c) Electron density on the longitudinal section of the Si CD (100) surface, i.e., the CD ($\bar{1}\bar{1}0$) surface, as obtained from KSDFT calculation. The slab configuration is shown in Fig. S3(b) of the Supplemental Material [50]. (d) Electron density differences of the Si CD (100) surface between OFDFT and KSDFT calculations. All of the calculations are performed in the equilibrium configuration obtained by KSDFT. The HC, WT, and TKK_{16}^s KEDFs are used in OFDFT. The MAREs, as defined in Eq. (12), of density differences are shown in the figures. The MAREs are calculated based on the whole electron density in the cell for a bulk CD Si and Si CD (100) surface.

V. CONCLUSION

In this work, we constructed two groups of TKKs with different cutoffs for metals and semiconductor systems, as a first step to find an optimal KEDF for metals and semiconductors. We further compared the performances of these kernels to validate how the real-space cutoff affects the properties of Al and Si systems. We systematically investigated several properties of the bulk and surface structures of Al and Si.

In general, the accuracy of TKKs increases with a larger cutoff. However, we found the TKK KEDFs with a short-range kinetic energy kernel ($\lambda_c = 8, 12$) yielded unreasonable stacking fault energies, surface energies, and vacancy formation energies for Al systems. Interestingly, we found that when the real-space cutoff of the TKK was larger than the distance between an atom and its next-nearest-neighbor atoms, the TKK was able to accurately characterize these properties and performed even better than the WT KEDF.

In conclusion, consideration of the interactions between an atom and its next-nearest-neighbor atoms is crucial for a nonlocal KEDF to distinguish the energy orderings among bulk structures, such as the fcc and hcp solid phases of Al, and CD and β -tin solid phases of Si. Furthermore, it helps to accurately predict the surface energies and point vacancies of Al and Si systems.

We found that the TKK_{16}^m and TKK_{16}^s kernels presented in this work gave reasonable results in all of the above tests. In addition, these kernels even performed better than the WT, WGC, and HC KEDFs in some aspects. For example, TKK_{16}^m yielded more accurate stacking fault energies than the WGC and WT KEDFs for the fcc structure of Al. The kernel performed better than the WT KEDF when dealing with the surface and vacancy formation energies in fcc Al. On the other hand, the TKK_{16}^s kernel yielded better vacancy formation energies than the HC KEDF for the CD Si structure. It exhibited reasonable accuracy in predicting the electron densities for bulk Al and Si systems, as well as the Al fcc (100) and Si CD (100) surfaces.

Despite the above advantages of the TKKs proposed here, we also encountered issues in the following three aspects. First, TKK^m 's, which are designed for metals, are not suitable for semiconductor systems such as Si. On the other hand, TKK^s 's (designed for semiconductors) are not accurate for metallic systems such as Al. This may be attributed to the different asymptotic behavior of KEDFs for semiconductors and metals [26], and we consider that machine learning is a potential tool to achieve a global KEDF for both metals and semiconductors. Second, the discrepancies between the electron densities obtained by OFDFT and KSDFT for semi-

conductors are considerably larger when compared to those observed in metals. In particular, for the CD phase of silicon, it is still challenging to pose a truncated KEDF kernel that shares the same accuracy as KSDFT. In the future, it would be interesting to test more solid phases of Si. Third, as expected, these differences tend to be substantially larger in surface systems than in bulk systems. However, we note that all of the WGC, HC, WT, and TKK KEDFs suffer from the above issues.

The force calculations with the usage of the TKK kernels have been implemented, and we found the current TKK KEDFs can be used to relax the bulk structure or even perform molecular dynamics simulations. However, the surface structures relaxed by the TKK KEDFs still deviate from the KSDFT results. One of the reasons is that the forces were not included in the residual function, and we expect the geometry relaxation and molecular dynamics functions be tested in future works.

To sum up, our investigation into the feasibility of employing nonlocal KEDFs in characterizing simple metal and Si systems enhances our comprehension of the forms and precision of KEDFs. Additionally, it sheds light on designing novel KEDFs. For future studies of other systems, such as molecules, insulators, and transition metals, etc, two challenges should be overcome. First, the generation of transferable local pseudopotentials should be addressed [45,60–62]. Second, more general KEDFs that can be applied to a variety of systems are needed.

ACKNOWLEDGMENTS

The work of L.S., Y.L., and M.C. was supported by the National Science Foundation of China under Grants No. 12074007 and No. 12122401. The numerical simulations were performed on the High-Performance Computing Platform of CAPT.

-
- [1] P. Hohenberg and W. Kohn, Inhomogeneous electron gas, *Phys. Rev.* **136**, B864 (1964).
 - [2] W. Kohn and L. J. Sham, Thermal properties of the inhomogeneous electron gas, *Phys. Rev.* **140**, A1133 (1965).
 - [3] Y. A. Wang and E. A. Carter, Orbital-free kinetic-energy density functional theory, *Theor. Methods Condens. Phase Chem.* **5**, 117 (2000).
 - [4] W. C. Witt, G. Beatriz, J. M. Dieterich, and E. A. Carter, Orbital-free density functional theory for materials research, *J. Mater. Res.* **33**, 777 (2018).
 - [5] K. M. Carling and E. A. Carter, Orbital-free density functional theory calculations of the properties of Al, Mg and Al–Mg crystalline phases, *Model. Simul. Mater. Sci. Eng.* **11**, 339 (2003).
 - [6] I. Shin and E. A. Carter, First-principles simulations of plasticity in body-centered-cubic magnesium-lithium alloys, *Acta Mater.* **64**, 198 (2014).
 - [7] H. L. Zhuang, M. Chen, and E. A. Carter, Prediction and characterization of an Mg–Al intermetallic compound with potentially improved ductility via orbital-free and Kohn–Sham density functional theory, *Model. Simul. Mater. Sci. Eng.* **25**, 075002 (2017).
 - [8] H. L. Zhuang, M. Chen, and E. A. Carter, Orbital-free density functional theory characterization of the β' -Mg₂Al₃ Samson phase, *Phys. Rev. Mater.* **2**, 073603 (2018).
 - [9] W. C. Witt, B. W. Shires, C. W. Tan, W. J. Jankowski, and C. J. Pickard, Random structure searching with orbital-free density functional theory, *J. Phys. Chem. A* **125**, 1650 (2021).
 - [10] M. Chen, L. Hung, C. Huang, J. Xia, and E. A. Carter, The melting point of lithium: An orbital-free first-principles molecular dynamics study, *Mol. Phys.* **111**, 3448 (2013).
 - [11] W. Mi and M. Pavanello, Orbital-free density functional theory correctly models quantum dots when asymptotics, nonlocality, and nonhomogeneity are accounted for, *Phys. Rev. B* **100**, 041105(R) (2019).
 - [12] Q. Xu, J. Lv, Y. Wang, and Y. Ma, Nonlocal kinetic energy density functionals for isolated systems obtained via local density approximation kernels, *Phys. Rev. B* **101**, 045110 (2020).
 - [13] Q. Liu, D. Lu, and M. Chen, Structure and dynamics of warm dense aluminum: A molecular dynamics study with density functional theory and deep potential, *J. Phys.: Condens. Matter* **32**, 144002 (2020).
 - [14] D. Kang, K. Luo, K. Runge, and S. Trickey, Two-temperature warm dense hydrogen as a test of quantum protons driven by orbital-free density functional theory electronic forces, *Matter Radiat. Extremes* **5**, 064403 (2020).
 - [15] Y. H. Ding, A. J. White, S. X. Hu, O. Certik, and L. A. Collins, *Ab Initio* Studies on the Stopping Power of Warm Dense Matter with Time-Dependent Orbital-Free Density Functional Theory, *Phys. Rev. Lett.* **121**, 145001 (2018).
 - [16] A. J. White, O. Certik, Y. H. Ding, S. X. Hu, and L. A. Collins, Time-dependent orbital-free density functional theory for electronic stopping power: Comparison to the Mermin–Kohn–Sham theory at high temperatures, *Phys. Rev. B* **98**, 144302 (2018).
 - [17] H. Xiang, Z. Wang, L. Xu, X. Zhang, and G. Lu, Quantum plasmonics in nanorods: A time-dependent orbital-free density functional theory study with thousands of atoms, *J. Phys. Chem. C* **124**, 945 (2020).
 - [18] K. Jiang, X. Shao, M. Pavanello *et al.*, Nonlocal and nonadiabatic Pauli potential for time-dependent orbital-free density functional theory, *Phys. Rev. B* **104**, 235110 (2021).
 - [19] L. A. Constantin, E. Fabiano, and F. Della Sala, Semilocal Pauli–Gaussian kinetic functionals for orbital-free density functional theory calculations of solids, *J. Phys. Chem. Lett.* **9**, 4385 (2018).
 - [20] L. A. Constantin, E. Fabiano, and F. Della Sala, Performance of semilocal kinetic energy functionals for orbital-free density functional theory, *J. Chem. Theory Comput.* **15**, 3044 (2019).
 - [21] K. Luo, V. V. Karasiev, and S. Trickey, A simple generalized gradient approximation for the noninteracting kinetic energy density functional, *Phys. Rev. B* **98**, 041111(R) (2018).
 - [22] K. Luo, V. V. Karasiev, and S. B. Trickey, Towards accurate orbital-free simulations: A generalized gradient approximation

- for the noninteracting free energy density functional, *Phys. Rev. B* **101**, 075116 (2020).
- [23] L.-W. Wang and M. P. Teter, Kinetic-energy functional of the electron density, *Phys. Rev. B* **45**, 13196 (1992).
- [24] E. Smargiassi and P. A. Madden, Orbital-free kinetic-energy functionals for first-principles molecular dynamics, *Phys. Rev. B* **49**, 5220 (1994).
- [25] Y. A. Wang, N. Govind, and E. A. Carter, Orbital-free kinetic-energy density functionals with a density-dependent kernel, *Phys. Rev. B* **60**, 16350 (1999).
- [26] C. Huang and E. A. Carter, Nonlocal orbital-free kinetic energy density functional for semiconductors, *Phys. Rev. B* **81**, 045206 (2010).
- [27] I. Shin and E. A. Carter, Enhanced von Weizsäcker Wang-Govind-Carter kinetic energy density functional for semiconductors, *J. Chem. Phys.* **140**, 18A531 (2014).
- [28] L. A. Constantin, E. Fabiano, and F. Della Sala, Nonlocal kinetic energy functional from the jellium-with-gap model: Applications to orbital-free density functional theory, *Phys. Rev. B* **97**, 205137 (2018).
- [29] W. Mi, A. Genova, and M. Pavanello, Nonlocal kinetic energy functionals by functional integration, *J. Chem. Phys.* **148**, 184107 (2018).
- [30] Q. Xu, Y. Wang, and Y. Ma, Nonlocal kinetic energy density functional via line integrals and its application to orbital-free density functional theory, *Phys. Rev. B* **100**, 205132 (2019).
- [31] X. Shao, W. Mi, and M. Pavanello, Revised Huang-Carter nonlocal kinetic energy functional for semiconductors and their surfaces, *Phys. Rev. B* **104**, 045118 (2021).
- [32] M. Chen, X.-W. Jiang, H. Zhuang, L.-W. Wang, and E. A. Carter, Petascale orbital-free density functional theory enabled by small-box algorithms, *J. Chem. Theory Comput.* **12**, 2950 (2016).
- [33] P. D. Haynes and M. C. Payne, Localised spherical-wave basis set for $O(N)$ total-energy pseudopotential calculations, *Comput. Phys. Commun.* **102**, 17 (1997).
- [34] M. Chen, G. Guo, and L. He, Systematically improvable optimized atomic basis sets for *ab initio* calculations, *J. Phys.: Condens. Matter* **22**, 445501 (2010).
- [35] M. Chen, G. Guo, and L. He, Electronic structure interpolation via atomic orbitals, *J. Phys.: Condens. Matter* **23**, 325501 (2011).
- [36] P. Li, X. Liu, M. Chen, P. Lin, X. Ren, L. Lin, C. Yang, and L. He, Large-scale *ab initio* simulations based on systematically improvable atomic basis, *Comput. Mater. Sci.* **112**, 503 (2016).
- [37] S. Kumar, B. Sadigh, S. Zhu, P. Suryanarayana, S. Hamel, B. Gallagher, V. Bulatov, J. Klepeis, and A. Samanta, Accurate parameterization of the kinetic energy functional for calculations using exact-exchange, *J. Chem. Phys.* **156**, 024107 (2022).
- [38] N. Metropolis, A. W. Rosenbluth, M. N. Rosenbluth, A. H. Teller, and E. Teller, Equation of state calculations by fast computing machines, *J. Chem. Phys.* **21**, 1087 (1953).
- [39] S. Kirkpatrick Jr., C. D. Gelatt Jr, and M. P. Vecchi, Optimization by simulated annealing, *Science* **220**, 671 (1983).
- [40] E. Fermi, Statistical method to determine some properties of atoms, *Rend. Accad. Naz. Lincei* **6**, 602 (1927).
- [41] C. F. Weizsäcker, Zur Theorie der kernmassen, *Z. Physik* **96**, 431 (1935).
- [42] M. Chen, J. Xia, C. Huang, J. M. Dieterich, L. Hung, I. Shin, and E. A. Carter, Introducing PROFESS 3.0: An advanced program for orbital-free density functional theory molecular dynamics simulations, *Comput. Phys. Commun.* **190**, 228 (2015).
- [43] H. J. Monkhorst and J. D. Pack, Special points for Brillouin-zone integrations, *Phys. Rev. B* **13**, 5188 (1976).
- [44] J. P. Perdew and A. Zunger, Self-interaction correction to density-functional approximations for many-electron systems, *Phys. Rev. B* **23**, 5048 (1981).
- [45] C. Huang and E. A. Carter, Transferable local pseudopotentials for magnesium, aluminum and silicon, *Phys. Chem. Chem. Phys.* **10**, 7109 (2008).
- [46] F. Murnaghan, The compressibility of media under extreme pressures, *Proc. Natl. Acad. Sci.* **30**, 244 (1944).
- [47] G. S. Ho, V. L. Lignères, and E. A. Carter, Introducing PROFESS: A new program for orbital-free density functional theory calculations, *Comput. Phys. Commun.* **179**, 839 (2008).
- [48] M. Gillan, Calculation of the vacancy formation energy in aluminium, *J. Phys.: Condens. Matter* **1**, 689 (1989).
- [49] N. Bernstein and E. B. Tadmor, Tight-binding calculations of stacking energies and twinnability in fcc metals, *Phys. Rev. B* **69**, 094116 (2004).
- [50] See Supplemental Material at <http://link.aps.org/supplemental/10.1103/PhysRevB.108.075158> for the detailed parameters used in the OFDFT and KSDFT calculations; the optimized coefficients for TKKs; the residuals of TKKs during the optimization; the numerical details about stacking fault energies; the bulk properties of Mg-Al alloys, HD and cbcc Si as obtained by KSDFT and OFDFT; the vacancy energies of fcc Al and CD Si; and the configurations of Al fcc (100) and Si CD (100) surfaces.
- [51] J. Tallon and A. Wolfenden, Temperature dependence of the elastic constants of aluminum, *J. Phys. Chem. Solids* **40**, 831 (1979).
- [52] M. Straumanis and C. Woodward, Lattice parameters and thermal expansion coefficients of Al, Ag and Mo at low temperatures. comparison with dilatometric data, *Acta Crystallogr. Sect. A* **27**, 549 (1971).
- [53] W. Triftshäuser, Positron trapping in solid and liquid metals, *Phys. Rev. B* **12**, 4634 (1975).
- [54] G. Watkins and J. Corbett, Defects in irradiated silicon: Electron paramagnetic resonance and electron-nuclear double resonance of the Si-E center, *Phys. Rev.* **134**, A1359 (1964).
- [55] S. Dannefaer, P. Mascher, and D. Kerr, Monovacancy Formation Enthalpy in Silicon, *Phys. Rev. Lett.* **56**, 2195 (1986).
- [56] C. Huang and E. A. Carter, Toward an orbital-free density functional theory of transition metals based on an electron density decomposition, *Phys. Rev. B* **85**, 045126 (2012).
- [57] Y. Ke, F. Libisch, J. Xia, L.-W. Wang, and E. A. Carter, Angular-Momentum-Dependent Orbital-Free Density Functional Theory, *Phys. Rev. Lett.* **111**, 066402 (2013).
- [58] Y. Ke, F. Libisch, J. Xia, and E. A. Carter, Angular momentum dependent orbital-free density functional theory: Formulation and implementation, *Phys. Rev. B* **89**, 155112 (2014).

- [59] W. Martienssen and H. Warlimont, *Springer Handbook of Condensed Matter and Materials Data* (Springer Science & Business Media, Berlin, 2006).
- [60] B. Zhou, Y. A. Wang, and E. A. Carter, Transferable local pseudopotentials derived via inversion of the Kohn-Sham equations in a bulk environment, *Phys. Rev. B* **69**, 125109 (2004).
- [61] F. Legrain and S. Manzhos, Highly accurate local pseudopotentials of Li, Na, and Mg for orbital free density functional theory, *Chem. Phys. Lett.* **622**, 99 (2015).
- [62] B. G. Del Rio, J. M. Dieterich, and E. A. Carter, Globally-optimized local pseudopotentials for (orbital-free) density functional theory simulations of liquids and solids, *J. Chem. Theory Comput.* **13**, 3684 (2017).